Available online at www.sciencedirect.com
ScienceDirect
Pattern Recognition 40 (2007) 563–577
PATTERN RECOGNITION
THE JOURNAL OF THE PATTERN RECOGNITION SOCIETY
www.elsevier.com/locate/patcog

Fast estimation of slopes of linear and quasi-linear structures in noisy background, using Fourier methods

P. Tsitsipis[a,*], A. Kontogeorgos[a], A. Hillaris[b], X. Moussas[b], C. Caroubalos[c], P. Preka-Papadema[b]

[a]*Department of Electronics, Technological Education Institute of Lamia, 35100 Lamia, Greece*
[b]*Department of Physics, University of Athens, 15783 Athens, Greece*
[c]*Department of Informatics, University of Athens, 15783 Athens, Greece*

Received 1 December 2005; accepted 19 April 2006

Abstract

We present a fast algorithm for slope detection on gray scale images, based on 2D Fourier transform and standard filters; this may be used for line or edge detection. Our approach is based on the calculation of "*energy*" per direction of the image, thus obtaining the "*energy spectrum on slope*" (θ). This exhibits local maxima at the points where θ equals the slopes of linear or quasi-linear segments within the image, yet it is not affected by their position within it. The process thus outlined has certain advantages as regards its efficiency of linear structure detection, compared to the Radon and Hough transforms. It was motivated by the study of astrophysical images (solar dynamic radio spectra) which necessitated the introduction of a method for fast extraction of "*drifting structures*", since they appear as linear or quasi-linear segments on these spectra.

Keywords: Line detection; Slope detection; Fourier transform Edge detection; Angular distribution

1. Introduction

The problem of the detection of linear or quasi-linear segments on gray scale images has incited a number of different methods aiming, mostly, at the calculation of slope and position of each and every linear structure in a given image (cf. for example Ref. [1]). The corresponding algorithms, such as Hough transform [2,3], Radon transform [4] and combinations thereof [5,6] are powerful tools yet of high computational complexity. More often than not their results are very good when a few linear segments are embedded within a relatively low noise background, yet their efficiency decreases when the number of the linear structures or the noise level increase; their performance is, also, adversely affected when the slopes of the linear segments are concentrated within a narrow range of values.

In this report we propose an algorithm based on fast Fourier transform (FFT); it draws upon the well established FFT advantages [7,8] as regards computational efficiency. The basic idea is the calculation of *energy density* as a function of angle; the peaks of *energy* per direction on the image indicate, in a statistical sense, the "*dominant*" slopes of linear or quasi-linear segments within the image.

The proposed method was motivated by the analysis of solar radio bursts observed by receivers with a broad band frequency range, and recorded simultaneously on a number of separate frequency channels. Their "*dynamic spectra*" are images depicting the variations in the bursts radiation intensity, represented by pixel brightness, in terms of time and logarithm of frequency which form, respectively, the *x*- and *y*-axis of the image. The frequency is characteristic of a certain layer of the solar atmosphere and proportional to the square root of the electron number density at that level; thus the logarithm of the frequency is proportional to the layer's height. This is due to the almost barometric (exponential) scaling of the coronal density near the solar surface.

* Corresponding author. Tel.: +30 2231039031; Fax: +30 2231037727.
E-mail address: tsitsipis@teilam.gr (P. Tsitsipis).

0031-3203/$30.00
doi:10.1016/j.patcog.2006.04.014

The solar radio bursts are broadly classified according to the form of their dynamic spectrum to "*drift bursts*" and "*continua*"; the former being narrow band structures drifting in frequency with time, the latter broadband forms covering most of the spectral range simultaneously. The *continua* family of bursts often exhibits "*fine structure*", which may become accentuated once the continuum background is suppressed (cf. for example [9,10]). Certain classes of fine structure features appear in form of groups of drifting elements. The importance of the detection of linear segments on dynamic spectra is twofold: Firstly, a number of drift bursts trace the path of an exciter ascending at an almost constant velocity within the solar atmosphere, thus forming linear segments on the dynamic spectra, secondly the terrestrial interference appears mostly in the form of constant frequency lines, i.e. parallel to the x-axis, which must be detected and duly eliminated.

In Section 2 the proposed method is outlined and particularly the basic theory is exposed (Section 2.1), the new method is described and compared to Radon and Hough methods (Section 2.2), the resolution of new method is derived (Section 2.3), the effect of noise (Gaussian, salt & pepper, missing pieces) is studied in Section 2.4 and restoration of linear structures out of a noisy environment is presented in Section 2.5. Finally, discussion and conclusions are presented in Section 3. The derivation of certain intermediate results is included, for clarity of presentation, in Appendix A and calculation of noise is done in Appendix B.

2. Outline of the method

2.1. The 2D Fourier transform of a linear segment

A linear segment of width D and length L, parallel to the x-axis, may by written as

$$f_0(x,y)=\varpi\left(\frac{x}{L}\right)\varpi\left(\frac{y}{D}\right),$$

$$\varpi(z)=\begin{cases}1, & |z|\leqslant\frac{1}{2},\\ 0, & |z|>\frac{1}{2}\end{cases} \tag{1}$$

the 2D Fourier transform is, approximately, another linear structure parallel to the y-axis (cf. Eq. (2)):

$$F_o(\xi_1,\xi_2)=L\cdot D\,\mathrm{sinc}(L\xi_1)\,\mathrm{sinc}(D\xi_2), \tag{2}$$

where

$$\mathrm{sinc}(x)=\frac{\sin(\pi x)}{\pi x}\quad\text{for } x\neq 0,$$

$$\mathrm{sinc}(0)=1. \tag{3}$$

In case the linear segment undergoes a rotation by φ the corresponding Fourier transform will also undergo a rotation by φ in the (ξ_1,ξ_2) domain (cf. Fig. 1):

$$f(x,y)=f_0(x\cos(\varphi)+y\sin(\varphi),-x\sin(\varphi)+y\cos(\varphi)),$$

$$F(\xi_1,\xi_2)=F_0(\xi_1\cos(\varphi)+\xi_2\sin(\varphi),\ -\xi_1\sin(\varphi)+\xi_2\cos(\varphi)), \tag{4}$$

where f, f_0 are two functions representing linear structures rotated by angle φ and F, F_0 the corresponding Fourier transforms. From Eqs. (2) and (4) we have

$$F(\xi_1,\xi_2)=\frac{\sin(L(\xi_1\cos(\varphi)+\xi_2\sin(\varphi)))}{\pi(\xi_1\cos(\varphi)+\xi_2\sin(\varphi))}\times\frac{\sin(D(-\xi_1\sin(\varphi)+\xi_2\cos(\varphi)))}{\pi(-\xi_1\sin(\varphi)+\xi_2\cos(\varphi))}, \tag{5}$$

which is the general form of the 2D Fourier Transform of a line segment.

2.2. The angular energy density

From Eqs. (2)–(5) and the Parseval's Theorem we have

$$\int\int|f(x,y)|^2\,\mathrm{d}x\,\mathrm{d}y=\int_{-\infty}^{\infty}\int_{-\infty}^{\infty}|F(\xi_1,\xi_2)|^2\,\mathrm{d}\xi_1\,\mathrm{d}\xi_2=2\int_0^{\pi}\mathrm{d}\theta\int_0^{\infty}|F(\xi,\theta)|^2\xi\,\mathrm{d}\xi,$$

$$\xi_1=\xi\cos(\theta),\quad \xi_2=\xi\sin(\theta), \tag{6}$$

where, in the last term of Eq. (6) we have changed from cartesian (ξ_1,ξ_2) into polar (ξ,θ) coordinates in Fourier space. We may define the "*angular energy density*" $(S(\theta))$ as follows:

$$S(\theta)=2\int_0^{\infty}|F(\xi,\theta)|^2\xi\,\mathrm{d}\xi=\frac{\mathrm{d}E}{\mathrm{d}\theta}$$

$$=2\int_0^{\infty}|F_0(\xi_1\cos(\omega)+\xi_2\sin(\omega),-\xi_1\sin(\omega)+\xi_2\cos(\omega))|^2\xi\,\mathrm{d}\xi$$

$$-\pi/2\leqslant\theta\leqslant\pi/2,\ \ \omega=\theta-\varphi. \tag{7}$$

The *angular energy density* represents the amount of *energy* (E) in the $(\theta,\theta+\mathrm{d}\theta)$ range and reaches a maximum for $\theta=\varphi+\pi/2$ (cf. Appendix A). This characteristic is exploited in the proposed process of *slope detection*.

Upon discretization the variables (x,y) are replaced by (m,n), (ξ_1,ξ_2) by (k,l) and (ξ,θ) by (v,u). We have [11,12]

$$F_{k,l}=\sum_{m=0}^{M-1}\sum_{n=0}^{N-1}f_{m,n}(\mathrm{e}^{-\mathrm{i}(2\pi/M)})^{mk}(\mathrm{e}^{-\mathrm{i}(2\pi/N)})^{nl},$$

$$E_{k,l}=\frac{1}{M\cdot N}|F_{k,l}|^2\ \Leftrightarrow\ \sum_{k=1}^{M}\sum_{l=1}^{N}E_{k,l}=E, \tag{8}$$

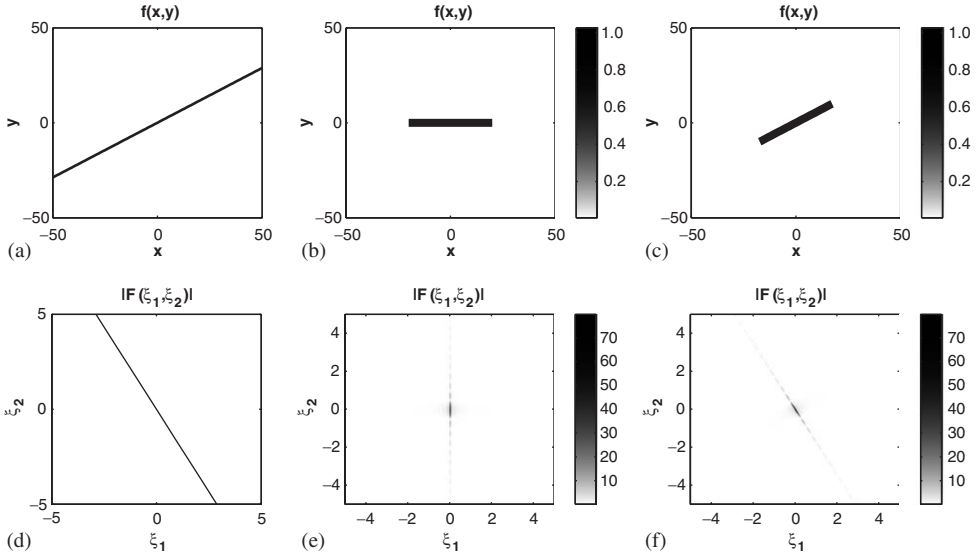

Fig. 1. Fourier transforms of linear structures: (panels a and d): a straight line, $f(x, y)$, and the corresponding 2D Fourier transform, $F(\xi_1, \xi_2)$. The same for an horizontal line segment (panels b and e) and for an arbitrary line segment (panels c and f). In all cases the 2D transform maps each segment to a line segment in Fourier space at right angle to the original.

where we have assumed that the original function and the corresponding 2D Fourier transform were sampled on a $M \times N$ grid. $F_{k,l}$ stands for the 2D discrete Fourier transform of $f(x, y)$ and $E_{k,l}$ for the *energy* on pixel (k, l), in Fourier space. In discrete polar coordinates, Eq. (8) assumes the form

$$E = \sum_u S_u = \sum_u \frac{2}{\pi N_B^2} \sum_{\upsilon=1}^{N_B} \upsilon \cdot E_{u,\upsilon}, \tag{9}$$

where we have taken $N_B = (N/2) - 1$, under the assumptions $M = N$ and $N_B \gg 1$ which do not result in any loss of generality, and S_u stands for the energy along the (discrete) direction u. We note that for the Fourier transform in polar form the sampling is not uniform as it is the case for the original function and its transform in cartesian coordinates (cf. Fig. 2), therefore the multiplier υ is used in the summation. Eq. (9) constitutes the definition of the *angular energy density* in discrete form, which is used henceforward throughout the text.

For comparison reasons we may define two function called "*angular distribution functions*" corresponding to Radon transform (S_R) and Hough transform (R_H). Radon Transform is given by the relation

$$F_R(\xi, \theta) = \int_{-\infty}^{\infty} \int_{-\infty}^{\infty} f(x, y)\delta(x \cos\theta + y \sin\theta - \xi)\mathrm{d}x\,\mathrm{d}y. \tag{10}$$

The selection of a threshold is necessary for the function $F_R(\xi, \theta)$ in order to enhance the line detection and eliminate

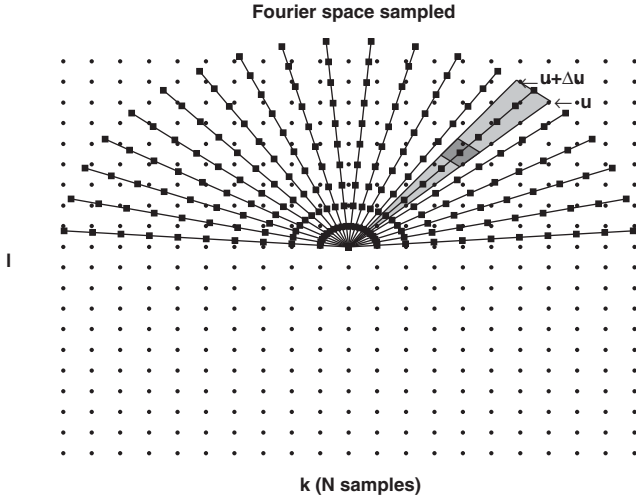

Fig. 2. Position of sampling marks in cartesian (points) and polar coordinates (square markers). The non-uniform sampling is obvious.

cluttering the 2D image. We have, hence

$$\widehat{F}_R(\xi, \theta) = \begin{cases} F_R(\xi, \theta) & \text{if } F_R(\xi, \theta) > T, \\ 0 & \text{if } F_R(\xi, \theta) > T, \end{cases} \tag{11}$$

where T is a threshold, and the *angular distribution function* (S_R) is

$$S_R(\theta) = \int_{-\infty}^{\infty} \widehat{F}_R(\xi, \theta)\,\mathrm{d}\xi. \tag{12}$$

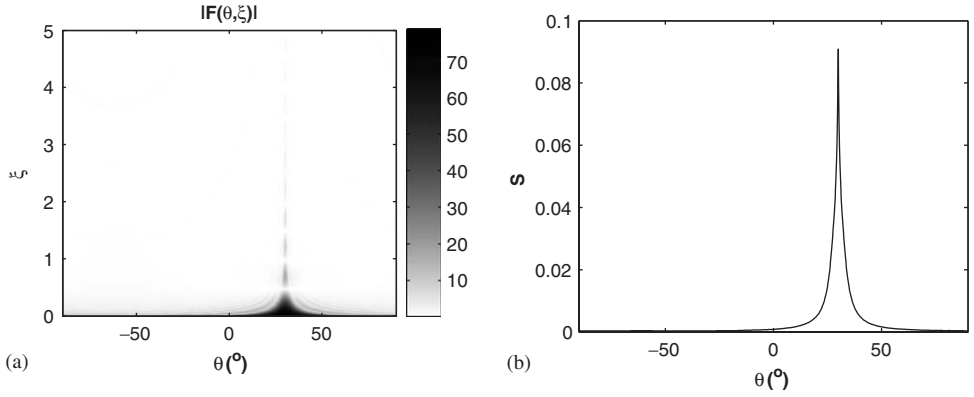

Fig. 3. Detection of a line segment within an image. Image of Fig. 1c is used. (a) Half Fourier space periodogram expressed in polar coordinates (θ, ξ). (b) Angular energy density (Integration of graph (a) on ξ).

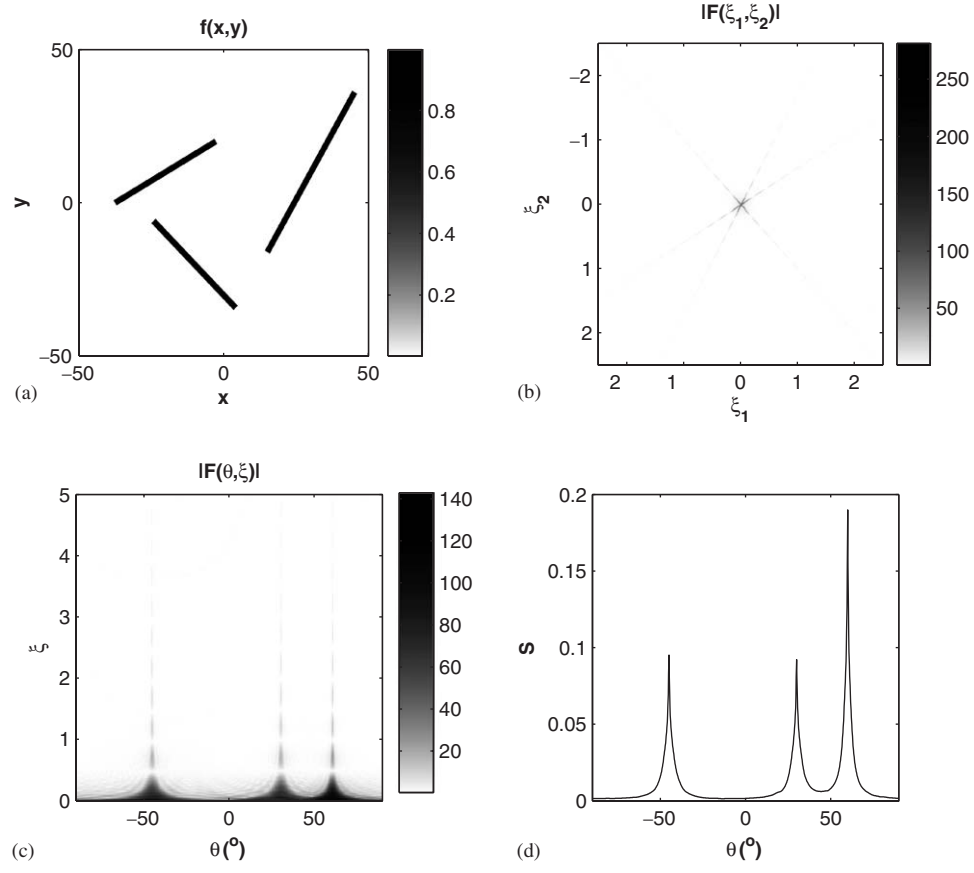

Fig. 4. Same as Fig. 3, but with three linear segments in the image.

The *angular distribution function* (S_H) is similarly obtained. These are used in the following paragraph to demonstrate the relative efficiency of the proposed algorithm compared to these two methods.

Examples of the computation of the *angular energy density* $(S(\theta)$ of linear segments on image are presented in Figs. 3 and 4. Results are compared with the *angular distribution functions* (S_H) and (S_R) on surrogate data comprising a number of images:

- An image with seven linear segments of various lengths (Fig. 5)

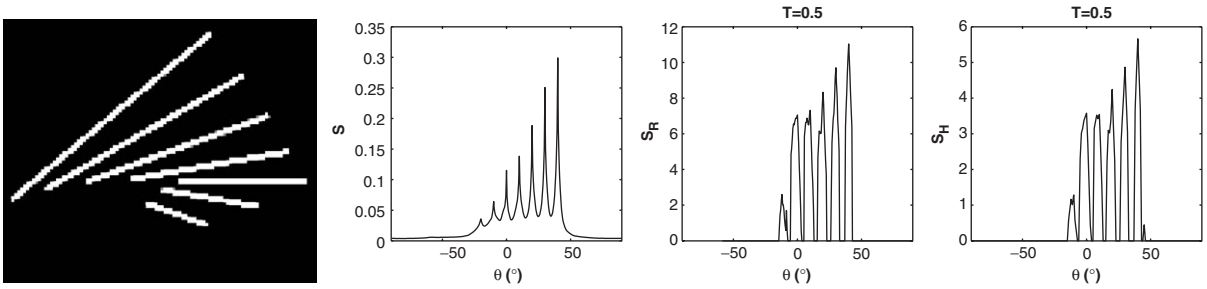

Fig. 5. Leftmost panel: a prototype image comprising a number of linear segments; it is used for comparison of the efficiency of the 2D-FFT method, proposed in this report, with the Hough and Radon transforms. Remaining three panels: angular spectra derived using our method (second panel from the Left), Radon transform (third panel) and Hough transform (rightmost panel), respectively.

- A selection of four prototype images subject to high pass filtering, for background suppression, (Fig. 6) end to *Sobel* edge enhancements (Fig. 7). These are
  - the "*pentagon*" image,
  - the "*house*" image,
  - the "*D15*" and "*D52*" *Brodaz* texture images.

All these images are characterized by a great number of linear segments which render them appropriate for the algorithm efficiency test.

We calculate angular energy densities, $S(\theta)$, $S_H(\theta)$, $S_R(\theta)$, using our method, Hough and Radon transforms, respectively. The necessity of adopting a threshold in the computation of $S_H(\theta)$, $S_R(\theta)$, in order to remove clutter from the diagrams, renders these two functions quite sensitive to the threshold level; it furthermore introduces a threshold dependent *selection* effect which manifests itself either by the appearance of spurious peaks or by the suppression of significant ones. In Figs. 6 and 7 the optimum threshold for each of $S_H(\theta)$, $S_R(\theta)$ has been selected by *trial and error* that we may have the best possible peak detection with the minimum clutter. In Fig. 6 we note that $S_H(\theta)$ fails to detect linear segments from high pass filtered images.

2.3. Resolution of the linear segment detection

Each line segment in an image is represented by a peak on the angular energy density plot of $S(\theta)$. The angle, $\delta\theta$, corresponding to the half peak value, in fact the "*peak width*", defines the resolution of the proposed method for the said segment; two similar peaks at a "distance" less than $\delta\theta$ are indistinguishable from each other. From the results of a large number of computations on prototype images with a single line segment (such as in Fig. 1), and varying length (L) and width (D) we may plot the resolution limit ($\delta\theta$) versus D/L (Fig. 8) which was found to follow the empirical relationship:

$$\delta\theta = 65.6(D/L), \tag{13}$$

where $\delta\theta$ is in degrees. Eq. (13) indicates that the resolution limit is proportional to the D/L ratio, hence a decrease in this ratio leads to an increase of the resolution. This, in turn, implies that we may improve the detection efficiency of the proposed method by means of high pass or edge detection filters; these may deform the original image, but they conserve slopes of linear segments and, furthermore, enhance the D/L ratio.

2.4. Background noise

The efficiency of our algorithm in the presence of additive white Gaussian, salt & pepper and missing pieces noise is examined and compared to Radon and Hough algorithms. For this comparison we use the prototype image of seven linear segments (Fig. 5) with added noise. The results are analyzed in the following subparagraphs (cf. also Figs. 9–11).

2.4.1. White Gaussian noise

The presence of additive white Gaussian noise (AWGN) in the image increases the mean and variance of background level of the *angular energy density*. In particular, additive white noise with zero mean and variance equal to σ^2, may raise the "*mean square error*" (henceforward MSE) of a noiseless image with maximum equal to unity, to $\mathrm{MSE} = \sigma^2$. Then, for the *angular energy density* (S_u) corresponding to angle u (Appendix B)

$$\mathrm{var}[S_u] = \frac{2\sigma^4}{3\pi^2}\frac{(N_B+1)(2N_B+1)}{N_B^3} \approx \frac{4\sigma^4}{3N_B\pi^2}, \quad N_B \gg 1. \tag{14}$$

This result suggests the use of a reasonable threshold (such as 5σ) in order to discriminate the spectral peaks representing line segments, from the noise spectrum. Hence we have $S_u \geqslant 10\sigma^2/\pi\sqrt{3N_B}$. For a more detailed presentation of this calculation cf. Appendix B.

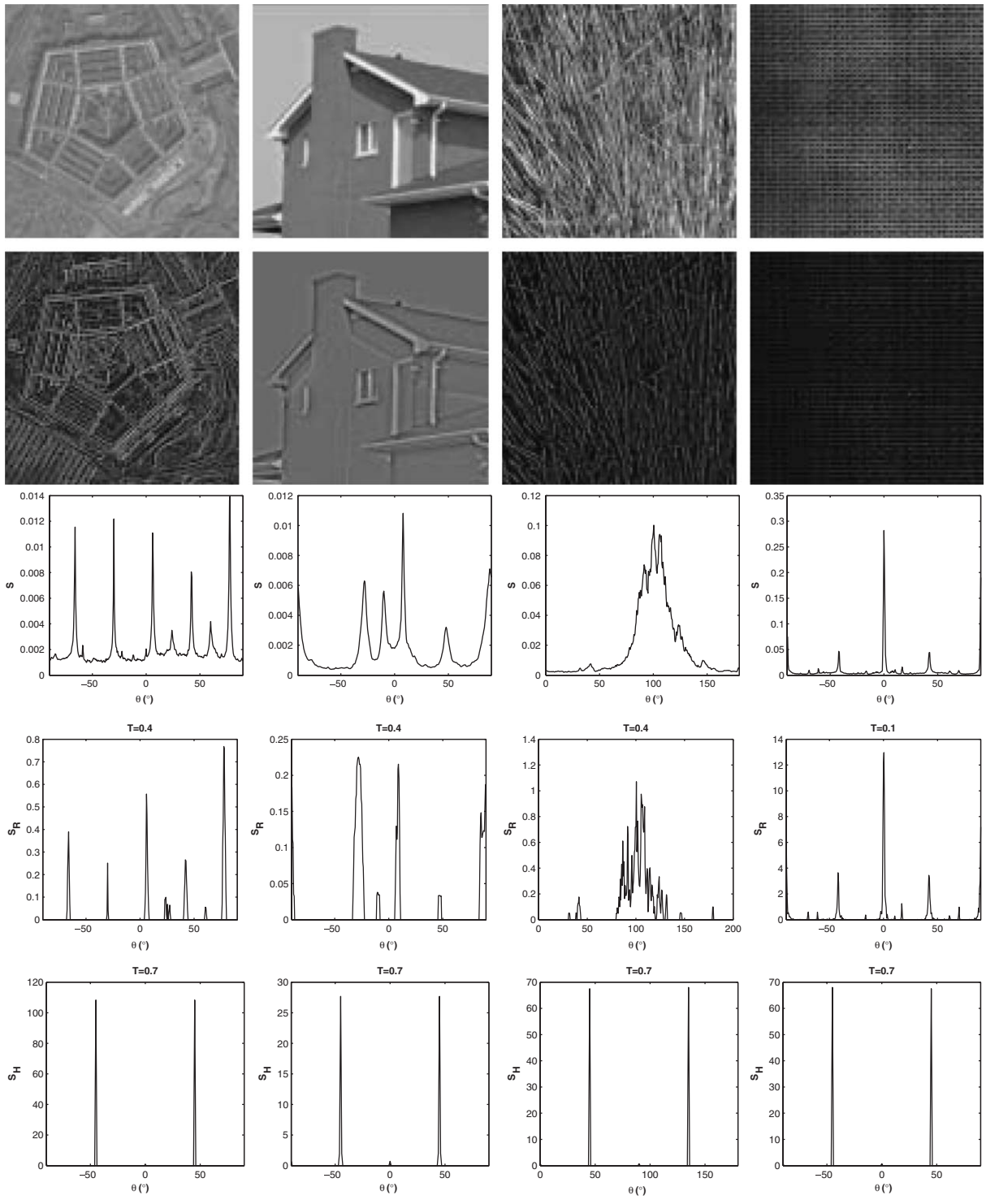

Fig. 6. Top panel (left to right): the images *pentagon*, *house*, *D15* and *D52 Brodatz* texture images. Second panel from top: same images as in top panel, submitted to an isotropic high pass filtering. Third panel: angular spectra of the filtered images derived using our method. Fourth panel: same spectra derived using Radon transform. Bottom panel: same spectra derived using Hough transform. The latter does not respond to the images.

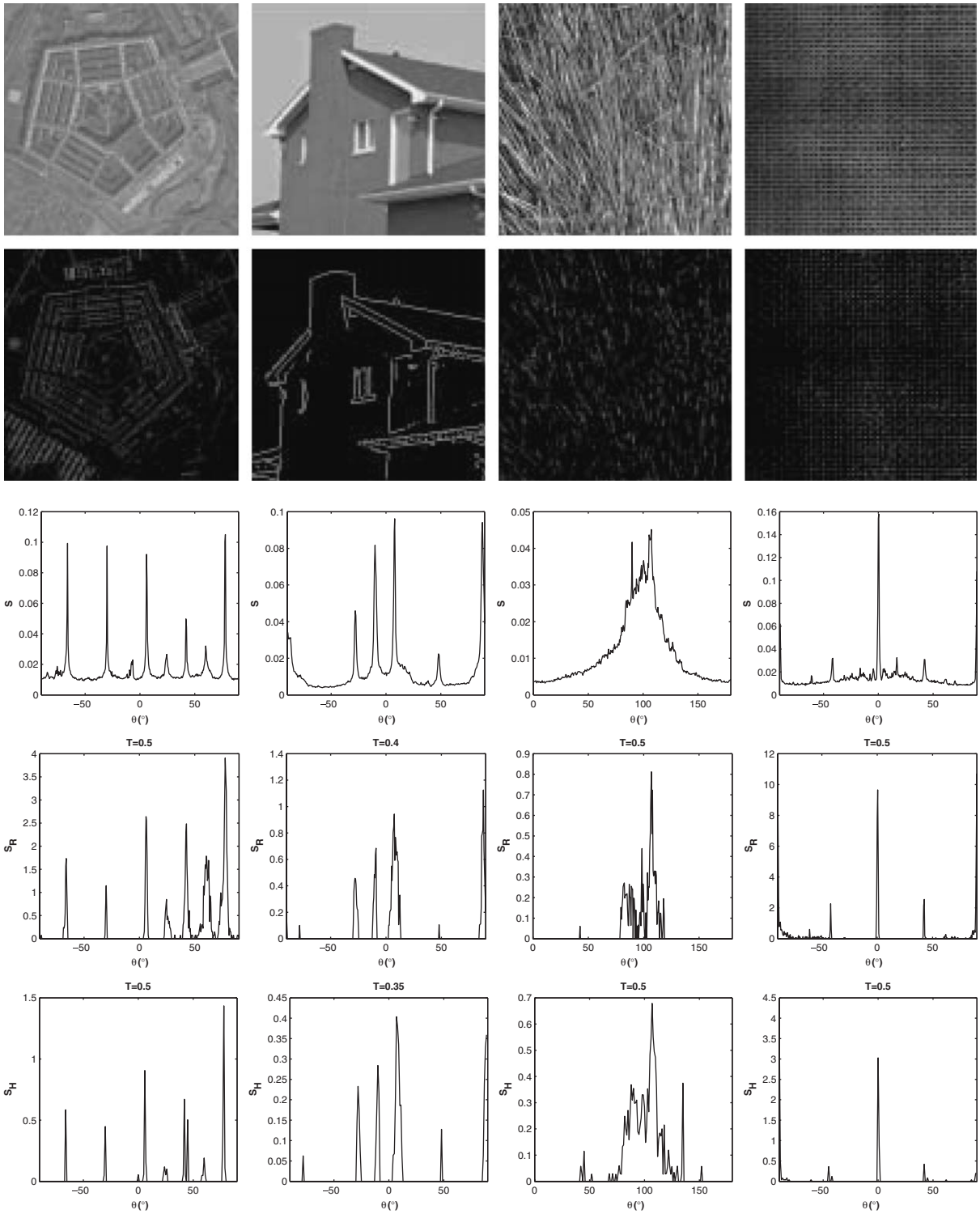

Fig. 7. Top two panels: same images as in Fig. 6, but filtered with a Sobel edge detection algorithm. Next three panels: angular spectra as in Fig. 6.

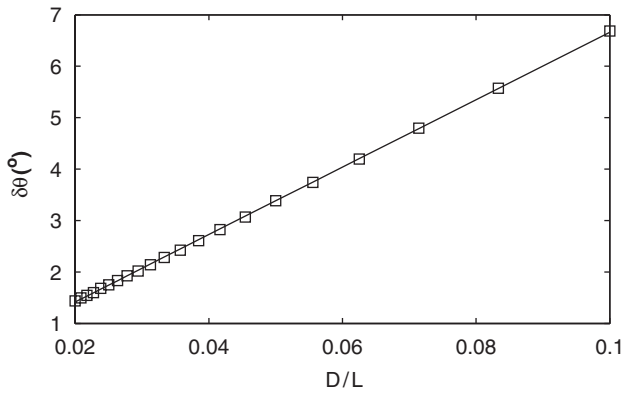

Fig. 8. Resolution of the slope detection method is determined by the *ridge width* of each segment, which is proportional to the ratio of width over length (D/L).

An example of the angular energy density of a "noisy" image for different signal to noise ratios (10, 5 and 0 dB) is exhibited in Fig. 9. The angular distribution function $S_H(\theta)$ is not responding to the original image but it may be enhanced by means of Sobel edge detection filtering. The same filter has been deemed necessary and has been applied in the computation of the Radon angular distribution function $S_R(\theta)$. As regards detection efficiency, when the noise level is low all three algorithms appear adequate to the task of edge detection. With increased back ground noise level though, spurious peaks appear in $S_H(\theta)$; further increase of the noise eliminates the shortest peaks of $S(\theta)$, $S_H(\theta)$, $S_R(\theta)$.

2.4.2. Salt & pepper noise

The angular energy density $S(\theta)$ and angular distribution functions $S_H(\theta)$ and $S_R(\theta)$, of the prototype image (Fig. 5) with added 5%, 15% and 50% salt & pepper noise are shown in Fig. 10. The angular distribution function $S_H(\theta)$ responds reasonably well to low and medium noise levels, but it exhibits spurious peaks at higher noise (50%). The Radon angular density, $S_R(\theta)$, responds well to the salt & pepper noise, yet the accuracy of the peaks deteriorates at high noise level. The angular energy density, $S(\theta)$, responds relatively well to all noise levels, missing only the shortest peaks (corresponding to the shortest linear segments) as the noise level increases.

2.4.3. Noise of missing pieces

We have, lastly, made a comparative test of the robustness of each of the three algorithms in the case of the missing pieces noise (cf. Fig. 11,) at low (5%), medium (15%) and high (50%) level. In the case of high noise level, the angular distribution functions $S_H(\theta)$ and $S_R(\theta)$ tend to miss certain peaks; this is not the case for the 2D Fourier based algorithm proposed in this report $(S(\theta))$.

2.5. Image directional filtering

We have, in the previous subsections, presented the line segment detection method including examples on surrogate data. In this section we formulate and apply the algorithm on actual images. These are solar *dynamic spectra*[1] hence the standard image coordinates x, y are replaced by time, t, and frequency, f (or logarithm of frequency, $\ln(f)$), in this case (Fig. 12).

More often than not some part of the image background needs be suppressed in order to enhance the linear structures before their detection, hence an initial stage of high pass filtering is, usually, included. As regards the dynamic spectra of solar radio bursts in particular, the detection of fine structure is customarily obtained by differentiation on time; this however, may introduce loss of information or distortion of the original signal. The use of directional filters to suppress interference at specific angles, such as $\theta = 0$ corresponding to fixed frequency terrestrial signals seems promising. Gaussian smoothing filters seem also appropriate to this task as they may also suppress slowly varying background components.

The algorithm for this directional filtering is briefly outlined as follows:

(1) An 1D Gaussian smoothing filter with a selected cut-off frequency f_s is designed; then the complementary high pass filter is calculated.
(2) The high pass filter is rotated to a specific angle, in order to suppress signals at this angle.
(3) In order to suppress aliasing we take the following steps:
   (a) points with a distance from the specified directional axis, smaller than $0.5/f_s$ are taken to lie on this axis;
   (b) points with a distance from the specified directional axis, greater than $0.5/f_s$ but smaller than $1/f_s$ take a value inversely proportional to the corresponding value on the axis;
   (c) all other points are set to zero.
(4) Lastly, we calculate the *angular energy density* of the filtered image. In case we detect a specific peak which we desire to suppress further we repeat the directional filtering process.

Fig. 12 is a solar radio burst dynamic spectrum, where we have successively applied high pass filters along the time and frequency axis and then our 2D Fourier based slope detection method.

[1] A *dynamic spectrum* is a method of representation of recordings by multichannel receivers. The x-coordinate is time, t, on the y-coordinate is the frequency of each receiving channel. The signal intensity from a channel of frequency f_n at time t_m, is represented by pixel brightness at (t_m, f_n); In Fig. 12 we have adopted a gray scale colour table, where white pixels correspond to the *background*, set to zero, and black pixels to maximum intensity.

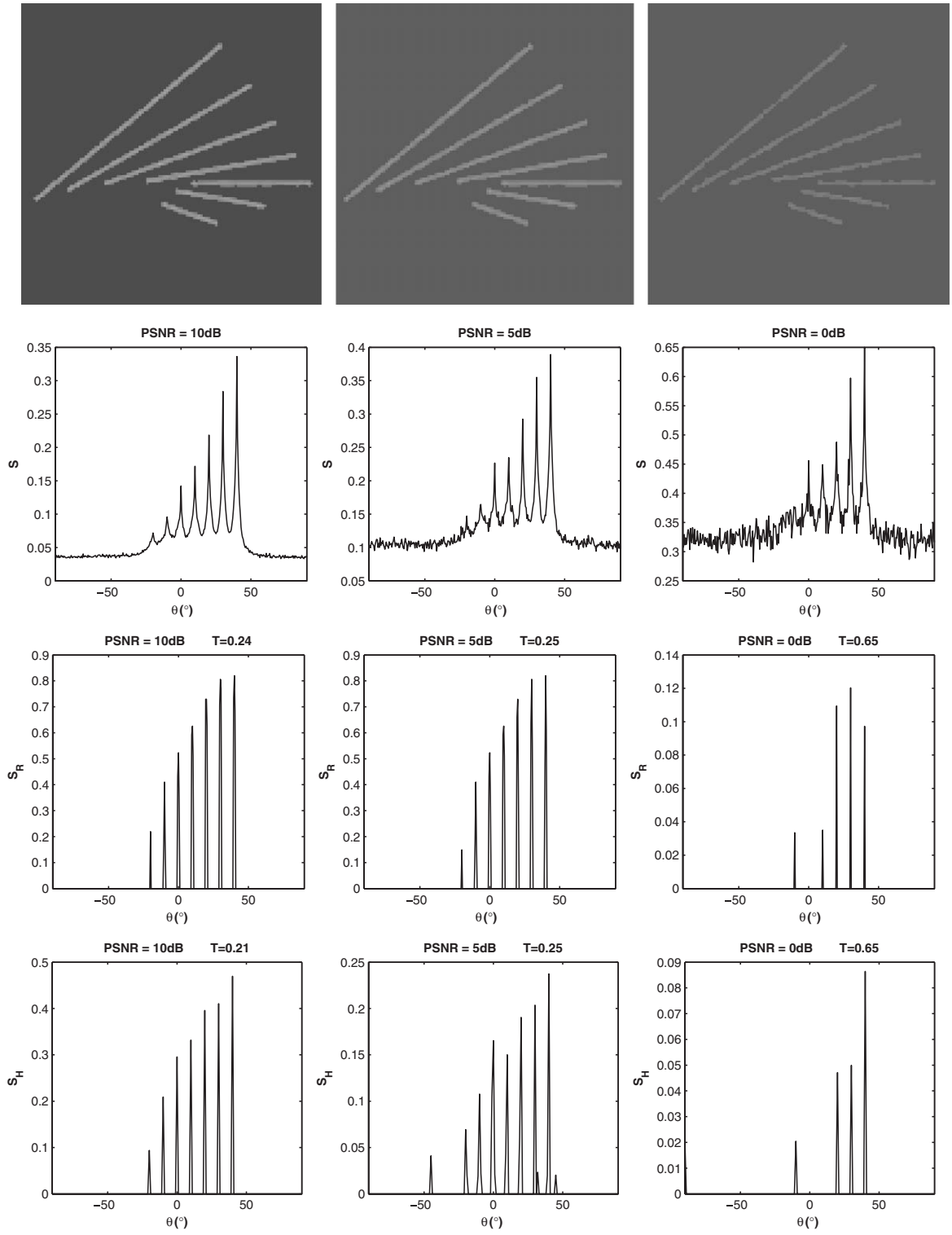

Fig. 9. Response of angular spectra to Gaussian noise. Top panel: the prototype image (cf. Fig. 5) with added Gaussian noise with PSNR 10, 5 and 0 db, respectively from left to right. Second panel: angular spectra of the noisy prototype image derived using our method. Third panel: angular distribution functions derived using Radon transform. Bottom panel: angular distribution functions derived using Hough transform.

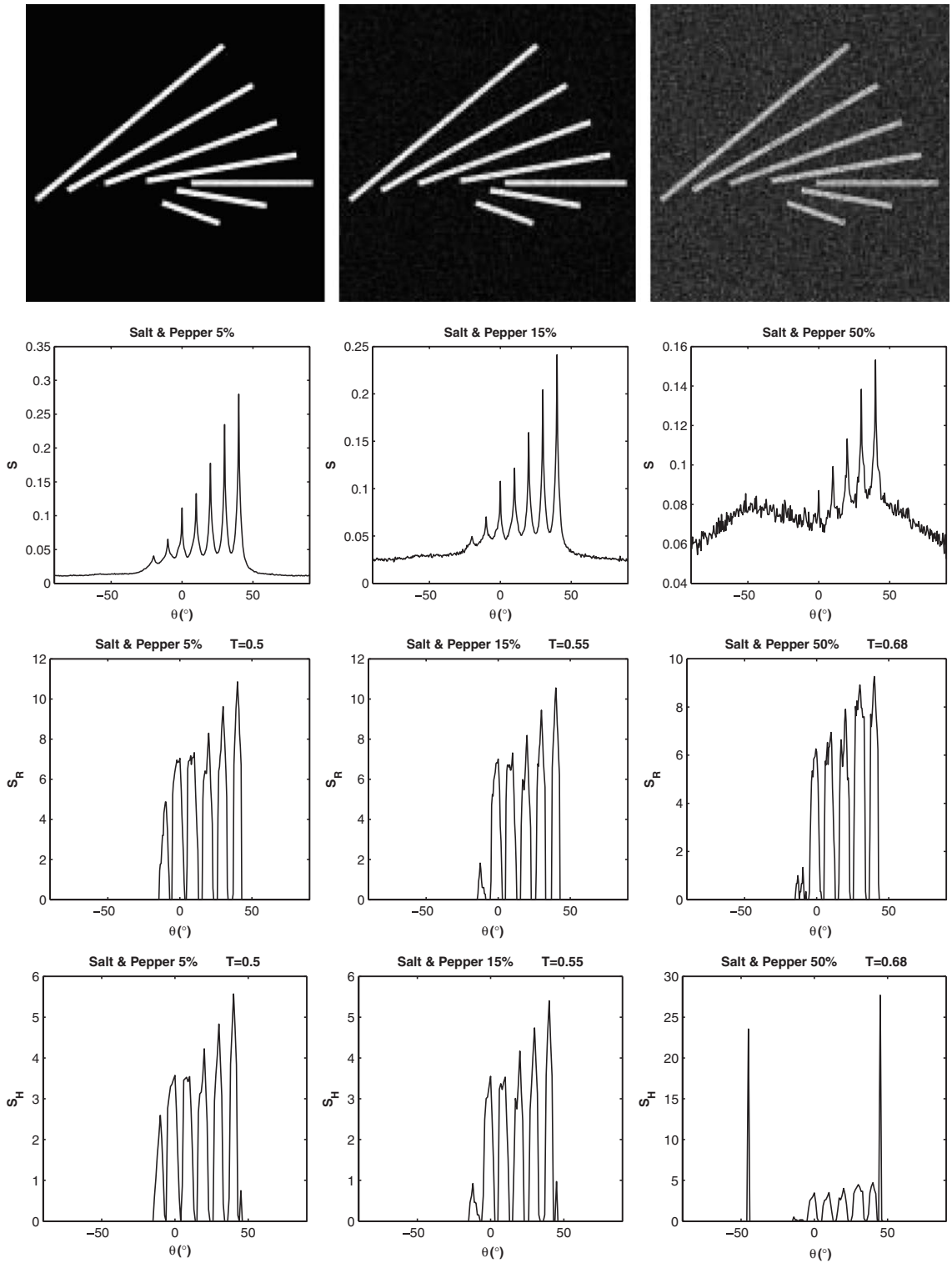

Fig. 10. Response of angular spectra to *salt & pepper* noise. The prototype image of Fig. 5 has been infected by 5%, 15% and 50% salt & pepper noise (top panel, left to right). In the second panel the corresponding angular spectra are depicted. In the third and bottom panels the corresponding distribution functions derived using Radon and Hough methods are depicted.

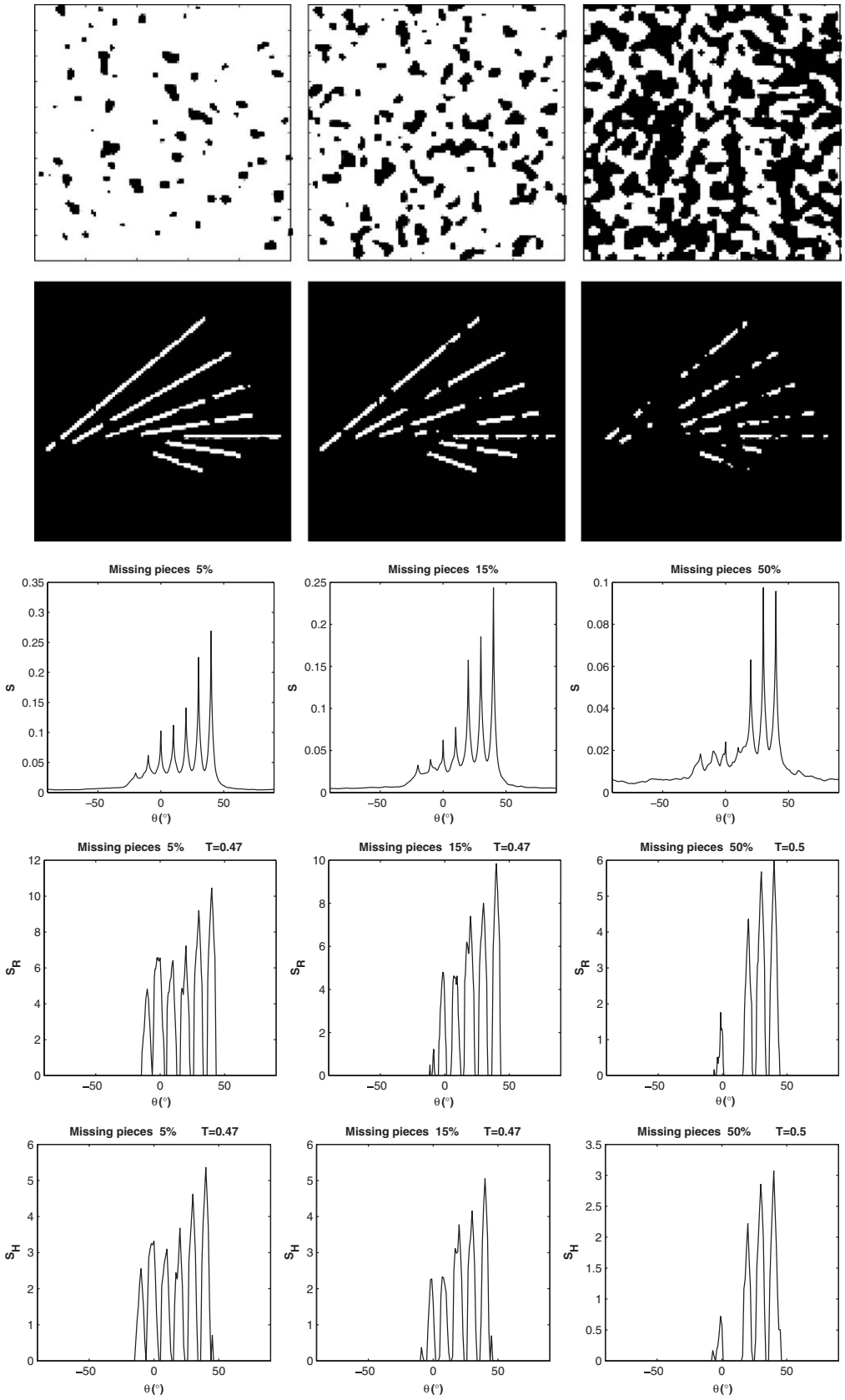

Fig. 11. Response of angular spectra to *missing pieces* noise. Test masks with 5%, 15% and 50% cut-off, respectively (top Panel) applied to the prototype image from Fig. 5 (second panel). Third panel: angular spectra of the masked image derived using our method. Fourth panel: same spectra derived using Radon transform. Bottom panel: same spectra derived using Hough transform.

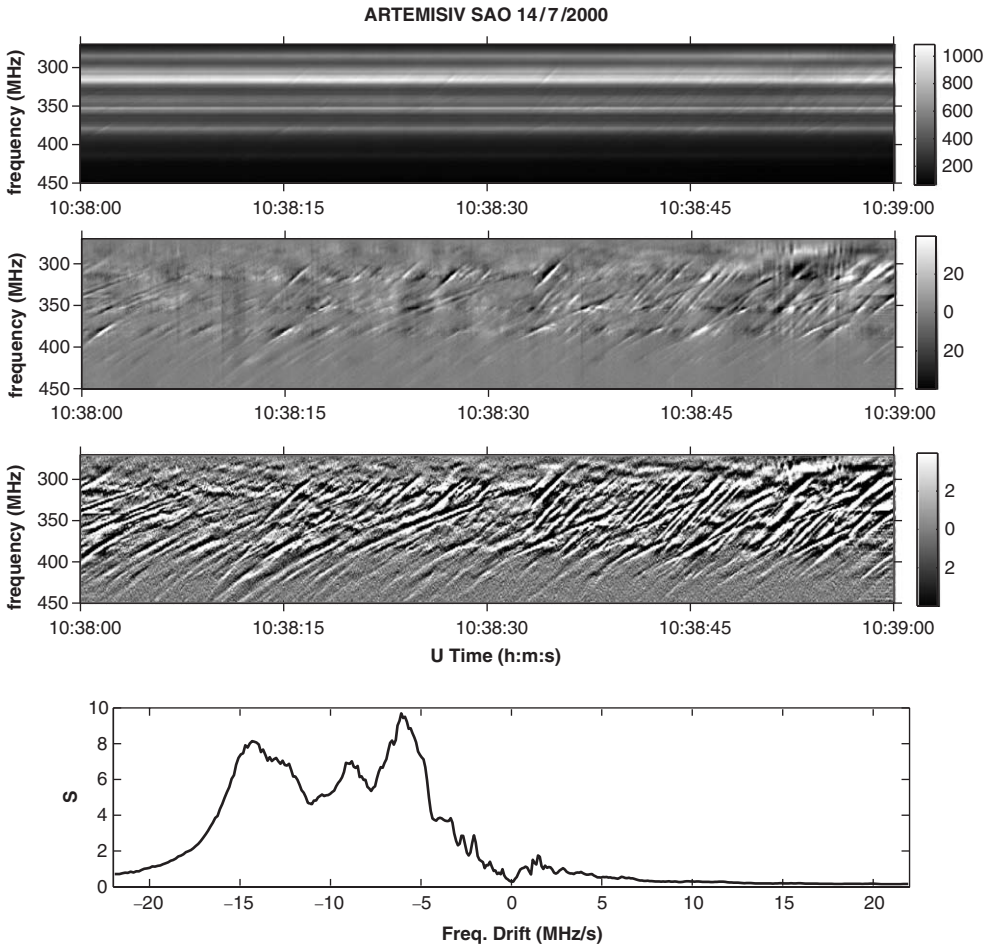

Fig. 12. Detection of linear segments corresponding to drifting structures on a dynamic spectrum recorded by the ARTEMIS-IV radio spectrograph [13] on the 14 July 2000. Top: dynamic spectrum of a solar continuum; the lines parallel to the time axis (x-axis) represent terrestrial interference. Second panel from the top: same images after a high pass filtering along the time axis; this has eliminated the interference and has suppressed the continuum enhancing the embedded fine structure. The latter consists of a *pulsating* vertical component and several drifting structures (known as intermediate drift bursts or *fibers*). Third panel from top: high pass filtering along the frequency axis (y-axis) has suppressed the *pulsating* component enhancing the *fibers*). Bottom: angular energy density of the filtered image.

3. Discussion and conclusions

In this report we present a fast algorithm for the detection of linear and quasi-linear structures in gray-scale images. Unlike previous attempts, this algorithm introduces the *angular energy density* and detects angular distribution of these structures in images; this statistical approach proves to be very useful in case of a great number of line segments. As is based on fast Fourier transform (FFT) methods, the computational efficiency and, in turn, the rate of estimation are high.

The noise immunity of the method is satisfactory since PSNR along a given direction angle is greater than a reasonably low threshold.

As regards the detection of solar radio burst fine structure the method proposed appears quite sensitive in slope detection. As already mentioned in Section 1 there is a direct correspondence between frequency and height in the solar atmosphere (*Corona*) hence the slopes of bursts on the time-frequency plane can be, almost immediately, indicate the corresponding velocities of their exciters. This suggests this method as a promising tool in the study of solar radio bursts.

Acknowledgments

The authors wish to thank Dr. Manolis Sangriotis for his suggestions and comments throughout this work. They, also, acknowledge many useful recommendations of the unknown referee who have improved significantly the quality of the original manuscript.

Appendix A. The angular energy density function $S(\theta)$ of a line segment

In this appendix we outline the derivation of the angular energy density function $S(\theta)$ of a line segment. The process is tedious but straight forward. From Eqs. (6) and (7) in

Section 2.2 we have

$$S(\theta) = 2\left(\frac{L\cdot D}{a\cdot b}\right)^2 \int_0^\infty \xi\, \mathrm{d}\xi\, \mathrm{sinc}^2(a\xi)\, \mathrm{sinc}^2(b\xi)$$
$$= 2\left(\frac{L\cdot D}{\pi^2 a\cdot b}\right)^2 \int_0^\infty (\mathrm{d}\xi/\xi^3)\sin^2(\pi a\xi)\sin^2(\pi b\xi)$$
$$= 2\left(\frac{L\cdot D}{a\cdot b}\right)^2 h(\xi,a,b), \quad (A.1)$$

where

$$a = L\,\cos(\theta-\varphi), \quad b = D\,\sin(\theta-\varphi). \quad (A.2)$$

We expand the numerator using standard trigonometric identities

$$\sin^2(\pi a\xi)\sin^2(\pi b\xi) = (1-\cos(2\pi b\xi)-\cos(2\pi a\xi))/4 + (\cos(2\pi(a-b)\xi) - \cos(2\pi(a+b)\xi))/8. \quad (A.3)$$

From (A.1), (A.2) and (A.3) we have

$$h(\xi) = \pi^2(b^2 Ci(2b\xi) + a^2 Ci(2a\xi))/2 - \pi^2(a+b)^2 Ci(2(a+b)\xi)/4 - \pi^2(a-b)^2 Ci(2(a-b)\xi)/4 - \pi(a\,\sin(2a\xi) + b\,\sin(2b\xi))/4\xi + \pi((a+b)\sin(2(a+b)\xi) + (a-b)\sin(2(a-b)\xi))/8\xi + (2\cos(2a\xi) - \cos(2(a+b)\xi) - \cos(2(a-b)\xi) + 2\cos(2b\xi) - 2)/16\xi^2, \quad (A.4)$$

where $Ci(x)$ is the *cosine integral* and is defined by the relation $Ci(x) = \gamma_E + \ln(x) + \int_0^x (\cos t - 1)\mathrm{d}t/t$ and γ_E is Euler's constant (=0.577215664...). We now let A and B, be the limits of $h(\xi)$ at zero and infinity, respectively. We thus have

$$\frac{(a\cdot b)^2}{(L\cdot D)^2}\, S(\theta) = B - A = \lim_{\xi\to\infty} h(\xi) - \lim_{\xi\to 0+} h(\xi), \quad (A.5)$$

where

$$A = -\left(\pi^2/4\right)\left(b^2\ln(a+b) + a^2\ln(a+b) + b^2\ln(a-b) + a^2\ln(a-b)\right) - \left(\pi^2/4\right)\left(-2b^2\ln(b) - 2a^2\ln(a) + 2ab\ln(a+b) - 2ab\ln(a-b)\right)$$
$$= \left(\pi^2/4\right)\left(2a^2\ln(a) + 2b^2\ln(b) - (a+b)\ln(a+b) - (a-b)\ln(a-b)\right) \quad (A.6)$$

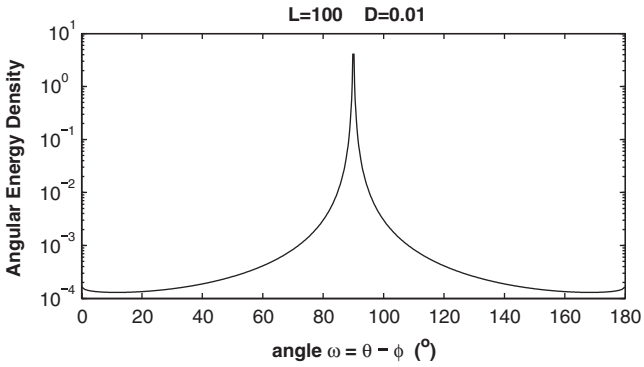

Fig. A.1. The function $S(\theta)$ (in logarithmic scale) versus $\omega = \theta - \varphi$, for $L = 100$ and $D = 1/100$.

and

$$B = \pi^3/8(2a^2\,signum(a) + 2b^2\,signum(b)) + \pi^3/8(-a^2\,signum(a+b) - b^2\,signum(a+b) - 2ab\,signum(a+b)) + \pi^3/8(-a^2\,signum(a-b) - b^2\,signum(a-b) + 2ab\,signum(a-b))$$
$$= \pi^3/8(2a^2\,signum(a) + 2b^2\,signum(b)) + \pi^3/8(-(a+b)^2\,signum(a+b) - (a-b)^2\,signum(a-b)). \quad (A.7)$$

In Eq. (A.1) we note that $h(\xi,a,b)$ is an even and symmetric function of a and b, so we may set $a>0$ and $b>0$ without loss of generality. Thus, we may have $a=|a|$, $b=|b|$ and $a+b=|a+b|$. From the symmetry we set $a>b$ without loss of generality, hence $a-b=|a-b|$. Substituting the simplified $h(\xi,a,b)$ into (A.6) and (A.7) we have real A and $B=0$. Therefore, from Eq. (A.5)

$$S(\theta) = \left(L^2D^2/2\pi^2a^2b^2\right)\left(-2a^2\ln|a| - 2b^2\ln|b| + (a+b)^2\ln|a+b| + (a-b)^2\ln|a-b|\right) \quad (A.8)$$

from Eq. (A.2) setting $\omega=\theta-\varphi$, $S(\omega)$ assumes the simplified form

$$S(\omega) = \left(1/2\pi^2\cos^2(\omega)\sin^2(\omega)\right)\left(-2L^2\cos^2(\omega)\ln|L\cos(\omega)| - 2D^2\sin^2(\omega)\ln|D\sin(\omega)| + (L\cos(\omega) + D\sin(\omega))^2\ln|L\cos(\omega) + D\sin(\omega)| + (L\cos(\omega) - D\sin(\omega))^2\ln|L\cos(\omega) - D\sin(\omega)|\right). \quad (A.9)$$

Graphical representation of Eq. (A.9) is shown in Fig. A.1 where a pronounced maximum at $\omega = \pi/2$ is formed.

Appendix B. Detection of linear structure in the presence of Gaussian noise

We calculate the variance of the periodogram in case of additive white Gaussian noise. Following [11] we have

$$\langle E_{\upsilon,u}\rangle = \sigma^2,$$
$$\mathrm{var}[E_{\upsilon,u}] = \sigma^4. \tag{B.1}$$

From Eq. (9) in Section 2.2 we have

$$\begin{aligned}\langle S_u\rangle &= \left(2/\pi N_B^2\right)\sum_{\upsilon=1}^{N_B}\langle \upsilon\cdot E_{u,\upsilon}\rangle = \left(2/\pi N_B^2\right)\sum_{\upsilon=1}^{N_B}\langle\upsilon\rangle\langle E_{u,\upsilon}\rangle\\ &= \left(2/\pi N_B^2\right)\sum_{\upsilon=1}^{N_B}\sigma^2\cdot\upsilon = \left(2\sigma^2/\pi N_B^2\right)\sum_{\upsilon=1}^{N_B}\upsilon\\ &= \left(2\sigma^2/\pi N_B^2\right)N_B(N_B+1)/2\\ &\cong \sigma^2/\pi\end{aligned} \tag{B.2}$$

hence

$$\begin{aligned}\langle S_u^2\rangle &= \left(4/\pi^2N_B^4\right)\left\langle\left(\sum_{\upsilon=1}^{N_B}\upsilon E_{\upsilon,u}\right)^2\right\rangle\\ &= \left(4/\pi^2N_B^4\right)\left(\sum_{\upsilon=1}^{N_B}\upsilon^2\langle E_{\upsilon,u}^2\rangle\right.\\ &\quad\left.+2\sum_{\upsilon_1=1}^{N_B-1}\sum_{\upsilon_2=\upsilon_1+1}^{N_B}\upsilon_1\cdot\upsilon_2\langle E_{\upsilon_1,u}\rangle\langle E_{\upsilon_2,u}\rangle\right)\\ &= \left(4/\pi^2N_B^4\right)\left(\sum_{\upsilon=1}^{N_B}\upsilon^2\langle E_{\upsilon,u}^2\rangle\right.\\ &\quad\left.+2\sum_{\upsilon_1=1}^{N_B-1}\sum_{\upsilon_2=\upsilon_1+1}^{N_B}\upsilon_1\cdot\upsilon_2\langle S_u\rangle^2\right)\\ &= \left(4/\pi^2N_B^4\right)\left(\sum_{\upsilon=1}^{N_B}\upsilon^2(\mathrm{var}[E_{\upsilon,u}]+\langle S_u\rangle^2)\right.\\ &\quad\left.+2\sum_{\upsilon_1=1}^{N_B-1}\sum_{\upsilon_2=\upsilon_1+1}^{N_B}\upsilon_1\cdot\upsilon_2\langle S_u\rangle^2\right)\\ &= \left(4/\pi^2N_B^4\right)\left(\sum_{\upsilon=1}^{N_B}\upsilon^2\mathrm{var}[E_{\upsilon,u}]+\sum_{\upsilon=1}^{N_B}\upsilon^2\langle S_u\rangle^2\right.\\ &\quad\left.+2\sum_{\upsilon_1=1}^{N_B-1}\sum_{\upsilon_2=\upsilon_1+1}^{N_B}\upsilon_1\cdot\upsilon_2\langle S_u\rangle^2\right)\\ &= \left(4/\pi^2N_B^4\right)\left(\sum_{\upsilon=1}^{N_B}\upsilon^2\mathrm{var}[E_{\upsilon,u}]+\langle S_u\rangle^2\right.\\ &\quad\left.\times\left(\sum_{\upsilon=1}^{N_B}\upsilon^2+2\sum_{\upsilon_1=1}^{N_B-1}\sum_{\upsilon_2=\upsilon_1+1}^{N_B}\upsilon_1\cdot\upsilon_2\right)\right)\\ &= \left(4/\pi^2N_B^4\right)\left(\sum_{\upsilon=1}^{N_B}\upsilon^2\mathrm{var}[E_{\upsilon,u}]+\langle S_u\rangle^2\left(\sum_{\upsilon=1}^{N_B}\upsilon\right)^2\right)\end{aligned} \tag{B.3}$$

and

$$\begin{aligned}\langle S_u\rangle^2 &= \left\langle\left(2/\pi N_B^2\right)\sum_{\upsilon=1}^{N_B}\upsilon E_{\upsilon,u}\right\rangle\\ &= \left(2/\pi N_B^2\right)\left(\sum_{\upsilon=1}^{N_B}\upsilon\langle E_{\upsilon,u}\rangle\right)^2\\ &= \left(2/\pi N_B^2\right)\langle E_{\upsilon,u}\rangle^2\left(\sum_{\upsilon=1}^{N_B}\upsilon\right)^2.\end{aligned} \tag{B.4}$$

From Eqs. (B.3) and (B.4) the variance of S_u for $N_B \gg 1$ is calculated:

$$\begin{aligned}\mathrm{var}[S_u] &= \langle S_u\rangle^2 - \langle S_u^2\rangle\\ &= \left[4/\pi^2N_B^4\right]\left(\sum_{\upsilon=1}^{N_B}\upsilon^2\mathrm{var}[E_{\upsilon,u}]+\langle E_{\upsilon,u}\rangle^2\left(\sum_{\upsilon=1}^{N_B}\upsilon\right)^2\right)\\ &\quad-\left[4/\pi^2N_B^4\right]\langle E_{\upsilon,u}\rangle^2\left(\sum_{\upsilon=1}^{N_B}\upsilon\right)^2\\ &= \left[4/\pi^2N_B^4\right]\sum_{\upsilon=1}^{N_B}\upsilon^2\,\mathrm{var}\,[E_{\upsilon,u}]\\ &= \left[4/\pi^2N_B^4\right]\sum_{\upsilon=1}^{N_B}\upsilon^2\sigma^4 = [4\sigma^4/\pi^2N_B^4]\sum_{\upsilon=1}^{N_B}\upsilon^2\\ &= \left[4\sigma^4/\pi^2N_B^4\right](N_B(N_B+1)(2N_B+1)/6)\\ &\cong \left(4\sigma^4/\pi^2N_B^4\right)\cdot(N_B^3/3)\\ &= 4\sigma^4/3\pi^2N_B.\end{aligned} \tag{B.5}$$

References

[1] A. Jain, Fundamentals of Digital Image Processing, Prentice-Hall, Englewood-Cliffs, NJ, 1989.
[2] R. Duda, P. Hart, Use of the Hough transform to detect lines and curves in pictures, Comm. Assoc. Comput. Mach. 15 (1972) 11–15.
[3] M. Attiquzzaman, M. Akhtar, A robust Hough transform technique for complete line segment description, Real Time Imaging 1 (1995) 419–426.
[4] A. Toft, Using the generalized Radon transform for detection of curves in noisy images, Proc. IEEE ICASSP 4 (1996) 2221–2225.
[5] R. Lo, W. Tsai, Gray-scale Hough transform for thick line detection in gray-scale images, Pattern Recognition 28 (1995) 647–661.
[6] R. Rangayyan, S. Krishnan, Feature identification in the time-frequency plane by using the Hough–Radon transform, Pattern Recognition 34 (2001) 1147–1158.
[7] S. Brantner, et al., High-speed tomographic reconstruction employing Fourier methods, Real-Time Imaging 3 (1997) 255–274.
[8] G.C. Ho, et al., A fast transform for the parametrisation of straight lines using Fourier methods, Real-Time Imaging 6 (1997) 113–127.
[9] C. Slottje, Atlas of Fine Structures of Dynamic Spectra of Solar Type IV-dm and Some Type II Radio Bursts, N.F.R.A Dwingeloo and Astronomical Institute of Utrecht, Utrecht, 1981.
[10] H. Aurass, K.-L. Klein, E.Ya. Zlotnik, V.V. Zaitsev, Solar type IV bursts spectral fine structures: observations, Astron. Astrophys. 410 (2003) 1001.
[11] J. Proakis, D. Manolakis, Digital Signal Processing, Prentice-Hall, Englewood-Cliffs, NJ, 1996.
[12] S. Theodorides, K. Koutroumbas, Pattern Recognition, Academic Press, New York, 1999.
[13] C. Caroubalos, D. Maroulis, N. Patavalis, J.-L. Bougeret, G. Dumas, C. Perche, C. Alissandrakis, A. Hillaris, X. Moussas, P. Preka-Papadema, A. Kontogeorgos, P. Tsitsipis, G. Kanellakis, The new multichannel radio spectrograph ARTEMIS IV/HECATE of the University of Athens, Exp. Astron. 11 (2001) 23–32.